LARGE SCALE SIMULATIONS OF SCATTERING OF WAVES BY RANDOM ROUGH SURFACES WITH APPLICATIONS IN MICROWAVE REMOTE SENSING AND WIRELESS COMMUNICATIONS

K.W. Lam*, Qin Li[+], L. Tsang*[+], K.L. Lai*, H.G. Wang*, L. Zhou[+], C.H. Chan* and L. Zheng*
*Wireless Communication Research Center, City University of Hong Kong, Hong Kong
[+]Department of Electrical Engineering, University of Washington, Seattle, WA, USA

1. INTRODUCTION

Scattering by random rough surfaces has been studied by analytic methods such as the Kirchhoff method and the small perturbation method. Numerical solutions of Maxwell equations were formidable in the past because in order to truly represent natural random rough surfaces, the profile must have many peaks and valleys. This require sample surface area of hundred or even thousands of square wavelengths. With the advent of fast computation methods, recently there has been intensive research to compute the exact numerical solution of Maxwell's equations for such problems. Over the past years, we have used the sparse matrix canonical grid method (SMCG) and the physics-based two-grid (PBTG) method that are used in matrix solvers in method of moment formulation [1-3]. The method has been extensively applied to large-scale and realistic 3D simulations of scattering by random rough surfaces. The method decomposes the integral equation full matrix into a sparse matrix, which represents near-field interactions, and the remainder of the matrix, which represents the non-near-field interaction part. The non-near-field part of the matrix is rewritten in a Taylor series by expanding the Green's function about a flat surface so that it can be calculated using FFTs. The computational complexity of the SMCG is O(NlogN) where N is the number of sampling points on the grid. Using low-cost Beowulf clusters [3], we have computed results up to several million surface unknowns. The simulations have been applied recently to practical problems such as microwave remote sensing of soils.

Recently, ultra-wideband (UWB) has caught much attention for the use in high-speed communication. In Feb 2002, the FCC approved the use of UWB with frequencies higher than 3GHz. The UWB communication is conveyed by the transmission of pulses with very narrow pulse duration in the order of nanoseconds and sub-nanoseconds. In this paper, we consider scattering of ultra-wideband pulses from random rough surfaces based on the exact solutions of Maxwell equations, instead of other heuristic statistical methods or approximate physical methods like ray tracing, which are widely used for propagation channel modeling in narrowband wireless communication. We illustrate numerical simulations of pulse shape, dispersion and fast fading multi-path when such ultra-wideband pulses are scattered by random rough surfaces. We compare the statistics of narrow band pulses as well as that of wideband pulses.

Together with the remote sensing discussed in this paper, we study the emissivities and backscattering coefficients of soil surfaces at microwave frequencies with this method. The goal is to determine the frequency dependence and polarimetric dependence of scattering and emission of soil using the same physical roughness parameters for a variety of soil moisture and roughness conditions. The simulation results are shown for the backscattering coefficients at the multi-incidence angles and at L & C frequency bands. The simulation results are also compared with the experimental measurements [4] with the fixed physical surface roughness parameters and soil moisture. For the passive remote sensing of soil surface, the emissivities are simulated at the observation angle of 50 degrees and at various conditions of soil moisture and surface roughness.

2. FORMULATION

Assume an electromagnetic wave from the medium 1 impinging on the rough interface of media 1 and 2, which is governed by a random height profile $z = f(x, y)$. Based on the Maxwell's equations, the fields on the surface should satisfy the surface integral equations.

$$\overline{E}_l(\bar{r})/2 + (-1)^l \int \hat{n}' \times \overline{H}_l(\bar{r}') i\omega\mu G_l dS' + (-1)^l P \int [(\hat{n}' \times \overline{E}_l(\bar{r}')) \times \nabla' G_l + \hat{n}' \cdot \overline{E}_l(\bar{r}') \nabla' G_l] dS' = \delta_{1l} \overline{E}^{inc}(\bar{r}) \quad (1)$$

$$\overline{H}_l(\bar{r})/2 + (-1)^{l-1} \int \hat{n}' \times \overline{E}_l(\bar{r}') i\omega\varepsilon_l G_l dS' + (-1)^l P \int [(\hat{n}' \times \overline{H}_l(\bar{r}')) \times \nabla' G_l + \hat{n}' \cdot \overline{H}_l(\bar{r}') \nabla' G_l] dS' = \delta_{1l} \overline{H}^{inc}(\bar{r}) \quad (2)$$

where the equations with index of $l=1$ and 2 are the surface integral equations in the media 1 and 2, respectively. G_1 and G_2 are the 3-dimensional Green's functions of free space and the lower dielectric medium, respectively. The integral $P\int$ denotes a Cauchy principal integral. The unit normal vector $\hat{n}'$ refers to primed coordinate and points away from the second medium. The function of δ_{1l} is zero if $l=2$ and one if $l=1$. The incident wave of $\overline{E}_i(\bar{r})$ and $\overline{H}_i(\bar{r})$ is tapered so that the illuminated rough surface can be confined to the surface area $L_x \times L_y$. The method of moments (MoM) is used to discretize the integral equations into the matrix equation. However due to the large number of surface unknowns, it is impossible to solve the matrix equation with a traditional solver. Instead of matrix inversion or Gaussian elimination method for large-scale rough surface simulation, the iterative technique is used in the paper with the sparse-matrix canonical grid method [1] to facilitate the matrix-vector multiplication and reduce the memory requirement. Furthermore, for the wave scattering from the lossy dielectric rough surfaces with large permittivity, we use a dense grid to sample the rough surface profile to increase the accuracy and to include fine-small structures of natural surfaces. The increased CPU time for the dense sampling is reimbursed by employing the physics-based two-grid method [1,2]. The SMCG and PBTG are used together to reduce the total CPU time and memory requirement. The computational complexity is O($N \log N$), where N is the number of grid points on the coarse grid. Parallel implementation is done using low cost Beowulf cluster [3].

The solved surface fields are calculated by solving the MoM equations. They are then used to calculate the bistatic scattering coefficients of $\sigma(\theta_i,\varphi_i;\theta_s,\varphi_s)$, where (θ_i,φ_i) are incident angle and (θ_s,φ_s) are scattering angle. The backscattering coefficients is defined as

$$\sigma^b(\theta_i,\varphi_i) = 4\pi\cos\theta_i\sigma(\theta_i,\varphi_i;\theta_i,\pi+\varphi_i) \tag{3}$$

The emissivity is calculated in terms of the following equation.

$$e(\theta_i,\varphi_i) = 1 - \int_0^{2\pi}\int_0^{\pi/2}\sigma(\theta_i,\varphi_i;\theta_s,\varphi_s)\sin\theta_s d\theta_s d\varphi_s \tag{4}$$

3. SIMULATION RESULTS FOR REMOTE SENSING

Fig. 1 and 2 show the backscattering coefficients obtained from the Monte Carlo simulations as a function of incident angles and the comparisons with the experimental measurements. The experimental results are from [4] and were taken from the same soil surface fields at two conditions of wet and dry soil moistures. The rms height and correlation length of the measured soil surface are 1.12cm and 8.4 cm, respectively. In the numerical simulation, we use these physical surface roughness parameters and soil moistures (relative permittivity) provided by [4] for both L and C band simulations. The rough surfaces are generated with the spectrum of the exponential correlation function that is also close to the description reported by the reference. The result in Fig. 1 is simulated from the wet condition of soil and Fig. 2 is from dry condition. The results in Fig. 1a and 2a are for L band and the results in Fig. 1b and 2b are for C band. The results in Fig. 2a give the best agreement between the simulations and measurements. Other figures also show the fairly good agreements between the simulations and the measurements.

The Fig. 3 shows the numerical simulation results for passive remote sensing of emissivity at the observation angle of 50 degrees. The simulations are the continuation of the work published in [2]. The relative permittivities of various soil moistures are calculated with the empirical formula in [5] at L band. The Fig. 3a is for the horizontal polarization and 3b is for the vertical polarization. The Figures show that the increased surface roughness will increase the emission of lower medium for the horizontal polarization. On the other hand, the effect is more complicated for the vertical polarization. One reason for that is the existence of the Brewster angle for vertical polarization. The results also show that surface roughness has large influence on the horizontal polarization emissivity while the vertical polarized emission is not very sensitive to the surface roughness.

4. SIMULATION RESULTS FOR WIRELESS COMMUNICATION

The UWB communication is conveyed by the transmission of pulses with very narrow pulse duration in the order of nanoseconds and sub-nanoseconds. To study the scattering of ultra-wideband pulses from random rough surfaces using Maxwell equations, we first find the scattering fields in frequency domain

and then use the Fourier transform to transfer to time-domain pulse. We consider two signal sources in time-domain in this paper. The first one is used in [6] as follows.

$$x(t) = [1 - 4\pi(\frac{t}{\tau_m})^2]\exp[-2\pi(\frac{t}{\tau_m})^2] \tag{5}$$

The time constant τ_m controls the bandwidth and central frequency of the signal. Its frequency response is

$$X(\omega) = \frac{\tau_m^3\omega^2}{8\pi^2\sqrt{2}}\exp(-\frac{\omega^2\tau_m^2}{8\pi}) \tag{6}$$

The second one is Gaussian pulse

$$x(t) = \exp[-(\frac{\Delta\omega t}{2})^2]\cos(\omega_0 t) \tag{7}$$

The parameter $\Delta\omega$ is the bandwidth and ω_0 is the central angular frequency of the signal. Its frequency response is

$$X(\omega) = \frac{1}{2\Delta\omega\sqrt{\pi}}\{\exp[-(\frac{\omega+\omega_0}{\Delta\omega})^2] + \exp[-(\frac{\omega-\omega_0}{\Delta\omega})^2]\} \tag{8}$$

After we solve the scattered fields in the frequency domain with numerical simulation, we can construct time-domain scattering fields with the Fourier transform

$$\vec{E}(\vec{r},t) = 2\,\mathrm{Re}\{\int_0^\infty d\omega X(\omega)\vec{E}(\vec{r},\omega)e^{-i\omega t}\} \tag{9}$$

In the numerical simulations, we use the tapered plane wave as the incident wave to illuminate the rough surface to avoid the infinite surface area. The illuminated surface area is 2,304 cm^2. The rough surface is generated with the Gaussian spectrum. The rms height is 0.6 cm and the correlation length is 6.0 cm. The relative dielectric constant of the lower medium is 3.66+i0.15. In Figure 4, we show the scattered field as a function of time. The signal source is given by equation (5) and the incident angle is 10 degrees. The time constant τ_m is taken as 0.1596 ns, which gives the central frequency of 5GHz. We simulate the scattered fields in frequency domain from 1GHz to 12GHz and then time-domain results are constructed with the Fourier Transform of equation (9). The scattered fields are observed in the vicinity of the center of rough surface at the height of 10 cm. Figure 4a shows that the shape of received pulse is similar to original signal source at one location while Figure 4b shows that the received pulse is different from the original one due to the dispersion of scattered fields at another location. Its cumulative distribution functions (CDF) at broadband frequency and at 5GHz are shown in Figure 5a and Figure 5b respectively. The fading statistics are particularly important for wireless communications [7-9]. In Figure 6, we show the similar results but the signal source is determined by equation (7). In this case, the central frequency is 6GHz and the scattered fields in the frequency domain are calculated from 4GHz to 8GHz. We plot one result with the similar shape of the incident signal in figure 6(a) and another one different from the incidence pulse in Figure 6(b) due to the dispersion.

5. REFERENCES

[1] L. Tsang, J.A. Kong, K.H. Ding, and C.O. Ao, *Scattering of Electromagnetic Waves, Vol. 2: Numerical Simulations*, Wiley Interscience, 2001

[2] Q. Li, L. Tsang, J.C. Shi, C.H. Chan, "Application of physics-based two-grid method and sparse matrix canonical grid method for numerical simulations of emissivities of soils with rough surfaces", *IEEE Trans. Geosci. Remote Sensing,* vol. 38, no. 4, pp. 1635-1643, July 2000.

[3] S.Q. Li, C.H. Chan, L. Tsang, Q. Li, and L. Zhou, "Parallel implementation of the sparse matrix/canonical grid method for the analysis of two-dimensional random rough surface (three-dimensional scattering problem) on a Beowulf system," *IEEE Trans. on Geosci. Remote Sensing*, vol. 38, pp.1600-1608, 2000

[4] Y. Oh, K. Sarabandi, and F.T. Ulaby, "An empirical model and an inversion technique for radar scattering from bare soil surfaces," *IEEE Trans. Geosci. Remote Sensing*, vol. 30, pp. 370-381, March 1992

[5] L. Tsang and R.W. Newton, "Microwave emissions from soils with rough surfaces," *J. Geophy. Res.*, vol. 87, no. 11, pp. 9017-9024, Oct. 1982.

[6] M.Z. Win and R.A. Scholtz, "Ultra-Wide bandwidth time hopping spread spectrum impulse radio for wireless multiple access communications," *IEEE Trans. on Communications*, vol. 48, no. 4, pp679-691, April 2000.

[7] D.S. Polydorou and C.N. Capsalis, "A new theoretical model for the prediction of rapid fading variations in an indoor environment", *IEEE Trans. on Vehicular Technology,* vol. 46, no.3, pp.748-754, August 1997.

[8] A. Abdi, "Comments on a new theoretical model for the prediction of rapid fading variation in an indoor environments", *IEEE Trans. on Vehicular Technology,* vol. 50, pp.331-334, January. 2001.

[9] H. Zhang, T. Udagawa, T. Arita and M. Nakagawa, "A statistical model for the small-scale multipath fading characteristics of ultra wideband indoor channel", *IEEE Conference on Ultra Wideband Systems and Technologies*, Baltimore, USA, May 2002.

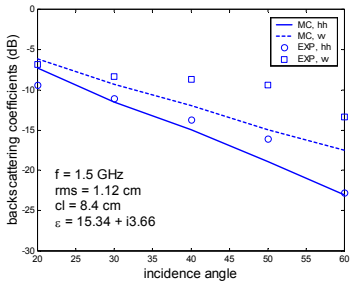

Fig. 1a

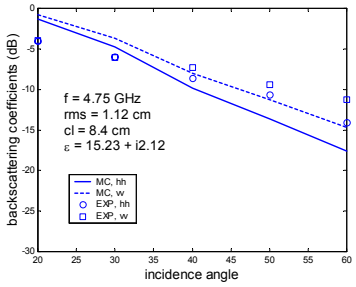

Fig. 1b

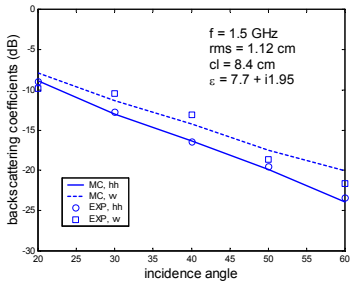

Fig. 2a

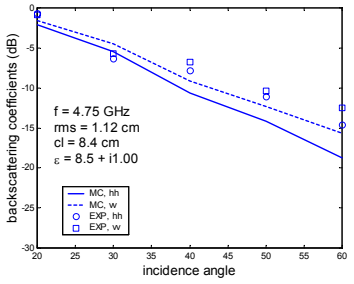

Fig. 2b

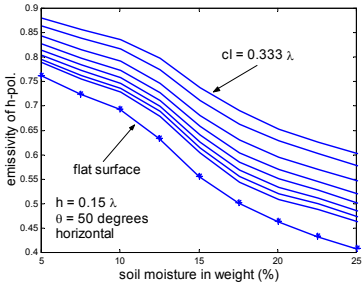

Fig. 3a

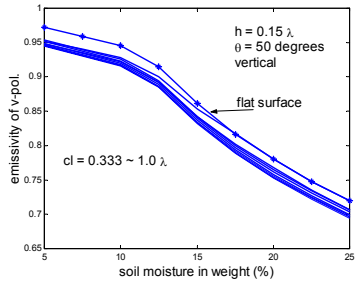

Fig. 3b

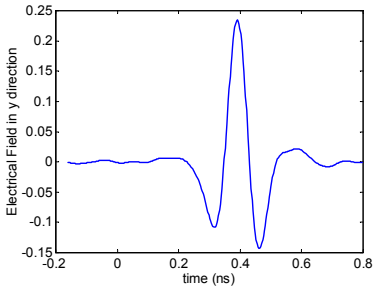

Fig. 4a

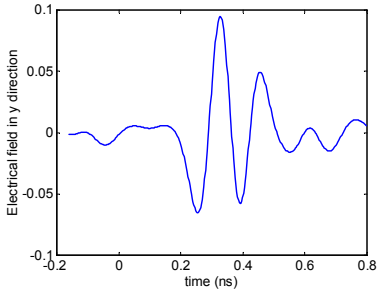

Fig. 4b

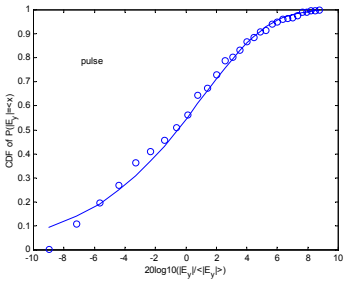

Fig.5a

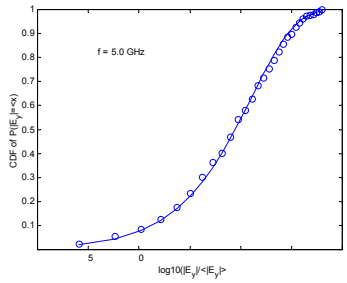

Fig. 5b

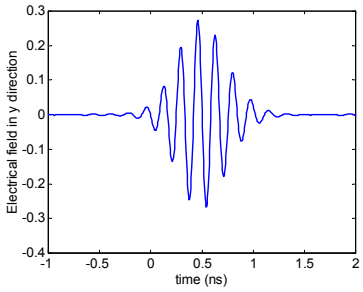

Fig. 6a

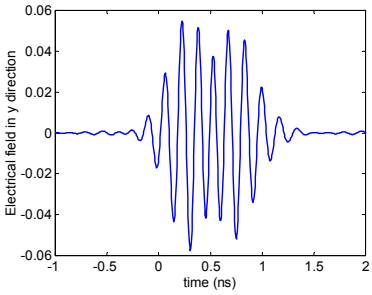

Fig. 6b